Oxygen Evolution on MoS_2: Activation through Edge Reconstruction

Naiwrit Karmodak* and Oliviero Andreussi*

Department of Physics, University of North Texas, Denton, TX 76203, USA

E-mail: naiwrit.karmodak@unt.edu; oliviero.andreussi@unt.edu

Abstract: The catalytic activity of MoS_2 edges for the oxygen evolution reaction is studied by means of *ab*-initio molecular dynamics simulations in the presence of a hybrid explicit/implicit description of the embedding of aqueous medium. Restructuring the zigzag (ZZ) edges with partial S-coverage is found to significantly reduce the reaction overpotential with resepct to the basal surface and the fully S-covered edges. These reconstructions are shown to be driven by the electrochemical adsorption of oxygen species and their strong binding affinity with the partially coordinated Mo atoms on the edge. Depending upon the reaction site and the restructuring mechanism, different concerted catalytic pathways for the thermal rearrangement of edge atoms and electrochemical charge transfer are observed, with minimum overpotential values varying between 0.4 and 0.8 V vs SHE. By performing a systematic exploration of the different configurations of the ZZ-edge, the catalytic activity of the system as a function of the S-coverage of the edge is characterized. A non-monotonic behavior is predicted with intermediate coverages (from 33% to 66%) showing the highest concentration of active sites.

TOC Graphic

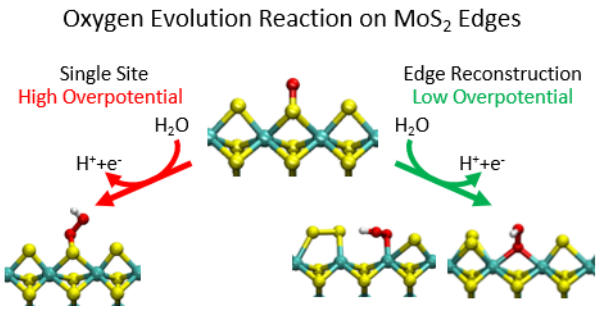

Introduction

Influenced by the significant success of two-dimensional (2D) materials in heterogeneous catalysis,[1] the screening of effective 2D electrocatalysts for water splitting have attracted immense attention.[2,3] While improving the rate of H_2 formation at the cathode is of prime importance for achieving better reaction efficiency,[4] the higher overpotential associated with the O_2 evolution reaction (OER) at the anode represents the main obstacle for the entire process:[5–7] sustainable technologies to produce fuel from water require a material capable of reducing the kinetic and thermodynamic barrier of O_2 oxidation. As a result of several efforts made in the recent years to identify suitable electrocatalysts for OER, the 2H structure of monolayer MoS_2 is found to be one of the stable 2D materials with simple synthetic techniques and proper alignment of the frontier energy bands with the water oxidation potential.[2,8–10] However, due to its inert basal surface, this compound shows limited reactivity towards the associated intermediates, resulting in an increased reaction overpotential.[11–13]

In order to enhance the catalytic activity of MoS_2, several activation pathways have been pursued. The most effective results have been obtained by varying its structural morphology, e.g. going from extended surfaces to nanostructured quantum dots,[14–16] to enhance the ratio of active edge sites. While this is a promising approach, the reactivity of electrocatalysts could also be tuned by modulating the interaction of its active sites with solvent molecules.[5–7] Recently, using continuum solvation models, we have shown that the catalytic performance and electrochemical stability of 2D materials for the H_2 evolution reaction (HER) could be favorably enhanced by tuning the solvent and electrochemical environment effects.[17] The

influence of solvent molecules enables an effective control on the stability of the polar reaction intermediates, thus allowing to improve the electrocatalytic performances of existing materials.[18,19]

Inspired by the recent experimental reports of vertically aligned edges as superior electrocatalysts for HER,[12,20] here we analyze the effect of surface morphology and explicit solvent interactions on the reactivity of MoS_2 edge sites for OER. Using unbiased first-principle approaches and molecular dynamics simulations, the factors that control the stability and reactivity of the MoS_2 basal surface and edges have been systematically studied. This allowed us to determine the origin of the overpotential for OER for the most relevant edge morphologies. It is found that modulating the surface S-coverage of the edges opens the possibility of a two-sites catalytic pathway, which results in overpotentials lower than those observed in conventional transition metal catalysts.

Computational Details

First principles density functional theory (DFT) calculations are performed using the revised VV10 density functional[21–23] and exploiting the Quantum Espresso simulation package.[24] Pseudo-potentials from the SSSP efficiency library[25,26] are used to model core electrons. Wavefunction and charge density cutoffs for the plane-wave basis sets of 40 and 400 Ry are chosen, respectively. For the Molecular Dynamics (MD) simulations, calculations are performed at the Γ point of the reciprocal Brillouin zone, whereas for the stability of the edges and the reaction free energy values, we have used the Γ-centered Monkhorst-Pack grid composed by 4 x 4 x 1 points. The electronic energy and force convergence thresholds are set to 10^{-7} eV and 10^{-2} eV/Å respectively. Moreover, electrostatic interactions along non-periodic directions are corrected using a parabolic correction scheme, as derived by Andreussi and Marzari[27] for simulations in vacuum or in continuum dielectric media.

Aqueous interactions are considered with a hybrid explicit/implicit solvation approach.

In this model, the water solution is divided into two regions: a bulk region, treated as a continuum dielectric environment and modelled using the Self-Consistent Continuum Solvation (SCCS) method,[28] and an interface region, modelled by a statistical ensemble of water bilayer configurations determined using *ab* initio molecular dynamics (AIMD) simulations.[29] Benchmark calculations for the interfacial free energy (γ) of monolayer MoS_2 using this hybrid approach show the best agreement with the experiments,[30–32] when compared to alternative full implicit or hybrid solvation models, as shown in Table T1 of the Supplementary Information (SI). Transition state energy values and the corresponding structures are determined using nudged elastic band (NEB) calculations,[33,34] where the solvent interactions on the transition state geometries are considered following the approach reported in Refs.[35,36]

AIMD simulations are performed at 350 K for 2-3 ps with canonical (NVT) ensemble using the velocity rescaling method to control the temperature fluctuations. A timestep of 1.0 fs is used. A rigid confining potential of 0.15 eV is applied at a distance of 4 Å away from the topmost water layer in order to restrict the movement of H_2O molecules away from the surface. The energies of the different systems are computed as the averages of single-point DFT calculations over 50 random snapshots extracted from the AIMD trajectories. Additional numerical details of the simulations are reported in SI.

The water oxidation mechanism and involved reaction free energies are determined using the computational hydrogen electrode (CHE) method.[7] While this approach represents an upper-bound to the correct interface free energies, the one-dimensional nature of the simulated edges and their intrinsic asymmetry hinder the use of more refined grand-potential schemes.[37]

Results and Discussion

Figure 1 shows the structural details of the different edges of MoS_2 considered in this study. Two types of edges are possible for MoS_2, denoted as the zigzag (ZZ) and armchair (AC)

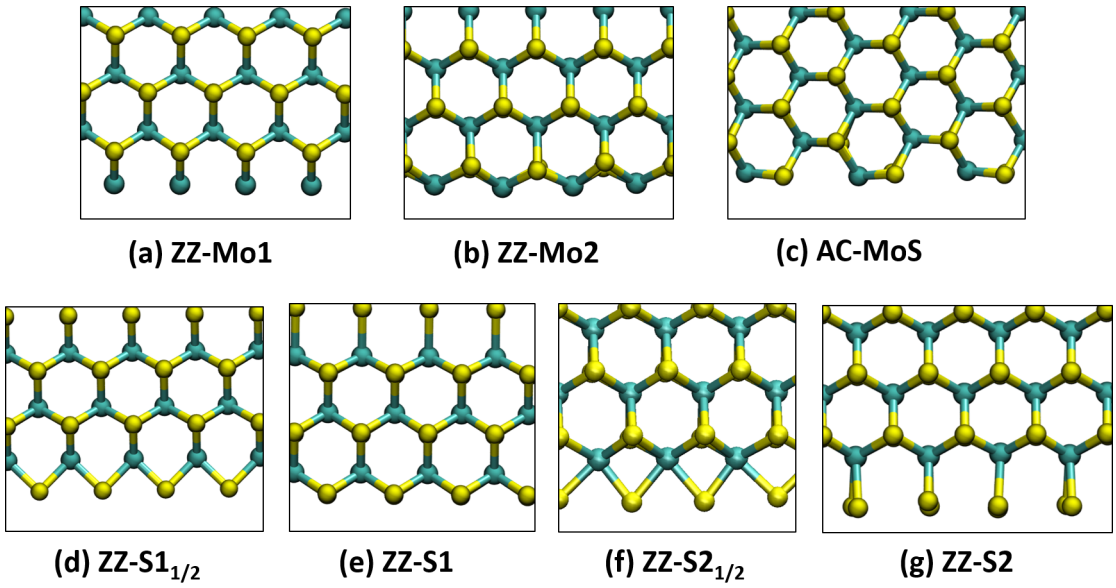

Figure 1: Structural arrangement of the main possible edges of MoS_2, with Mo atoms reported in cyan and S atoms in yellow. Following the standard nomenclature for graphene edges, both zigzag (ZZ) and armchair (AC) edges have been considered. The ZZ-S1$_{1/2}$ and ZZ-S2$_{1/2}$ represents the S-terminated edges obtained from ZZ-Mo1 and ZZ-Mo2, respectively, with a 50% edge coverage of sulphur atoms. ZZ-S1 and ZZ-S2 are the corresponding sulphur terminated edges with 100% S-coverage.

edges.[38,39] While a single configuration exists for the AC-MoS edge, the ZZ edges are further classified into Mo-edges or S-edges depending upon the element with dangling valences present at the edges. In a minimal unit cell, two possible Mo terminated structures, ZZ-Mo1 and ZZ-Mo2, can be considered, corresponding to a 0% S-coverage of the edge. Starting from these edges, we can generate four different S edges: ZZ-S1$_{1/2}$ and ZZ-S2$_{1/2}$ with 50% S-coverage respectively, and ZZ-S1 and ZZ-S2 edges with 100% S-coverage respectively. Intermediate values of S-coverage can in principle be generated as a combination of these minimal cell structures and have not been explicitly considered in this study.

The stability of the edges in vacuum and in solutions are obtained at varying S chemical potentials using an approach similar to the one reported by Joo et al.,[40] but including the presence and statistical nature of explicit solvent molecules in the simulation (as detailed in Supporting Information section S-II and S-III).

The calculated formation energies, as compared to the one of the MoS_2 basal surface,

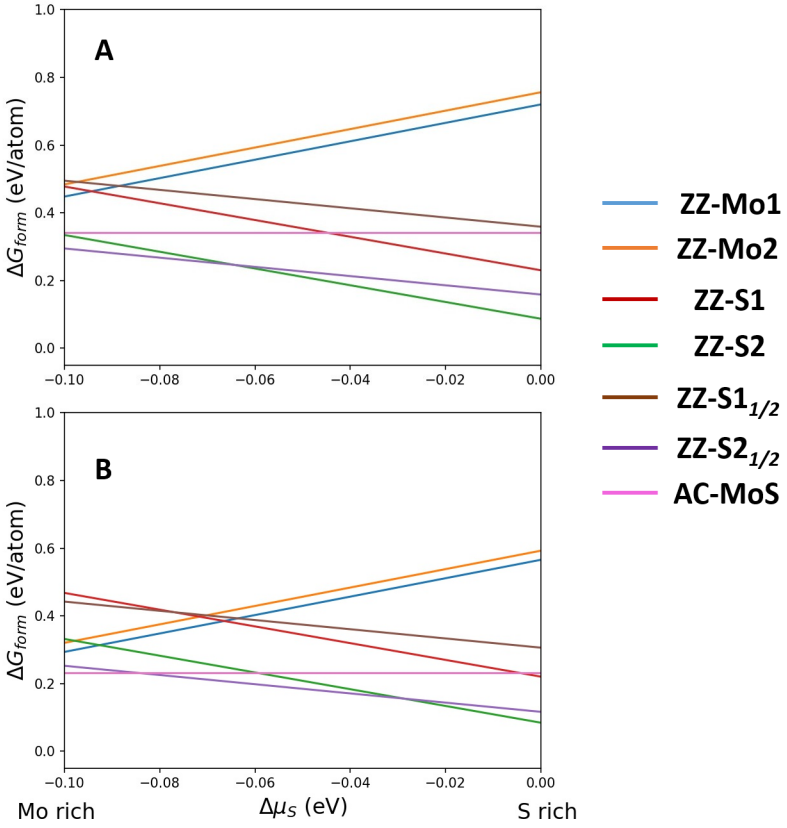

Figure 2: Formation free energies (ΔG_{form}) for the different edges shown in Figure 1 as a function of S chemical potential (μ_S). The values are reported with respect to the MoS_2 basal surface for simulations in vacuum (A) and in the presence of an aqueous embedding environment (B). The most probable arrangements of the edges in aqueous solvent are determined by means of MD simulations at 350K for 4 ps time scale. $\mu_S = 0$ denotes the S-rich conditions, when the value is equivalent to the most stable sulphur allotrope. For Mo-rich conditions, the corresponding μ_S values are determined from the $\mu_{MoS_2}{}^{bulk}$ and the most stable solid phase of molybdenum.

are plotted in Figure 2 as a function of increasing S chemical potential. The change in stability for the different edges is univocally determined by the ratio of Mo vs. S atoms in the structure. In particular, a decrease/increase in stability is predicted for S-poor/S-rich edges, while the AC edge, with an ideal 1:2 ratio, show no changes with S chemical potential. In vacuum (Figure 2A), the most stable edges are the ZZ-S2 ones, with the 50% S-coverage becoming the most stable at low S chemical potentials.

Although the trends in stability are not affected by the presence of a solvation environment, the relative stability of the different edges show significant variations, reflecting differences in the strength of the interaction with the solvent molecules (Figure 2B).

In particular, the oxygen atoms of water molecules appear to strongly interact with uncoordinated Mo atoms, providing a larger stabilization to S-poor structures, such as the Mo-terminated edges and the AC edge. Among the S-rich edges, structures with 50% S-coverage are slightly stabilized by the presence of water molecules, while a negligible effect is seen on 100% S-coverage edges. The net result of these solvation effects is that for low S chemical potential, the AC structure shows the lowest formation energy, while the ZZ-$S2_{1/2}$ structure is stable for intermediate values of the S chemical potential, and the stability of the ZZ-$S2_{1/2}$ edge is reduced to only S rich environments. Among the different edges, ZZ-Mo1 and ZZ-$S2_{1/2}$ edges are found to show different structural variations in vacuum depending upon the size of the simulation cell (Figure S3 and S4, SI). The most stable structural polymorphs are chosen for both the edges to study the aqueous stability and catalytic performance. By considering larger supercells, intermediate values for the S-coverage of the ZZ-S2 edge can be considered, leading to a smoother transition in stability as a function of the S chemical potential, possibly competing with the AC edge in Mo rich conditions.

Apart from affecting the stability of the different edges, the interaction of uncoordinated Mo atoms with the oxygen atom of the solvent molecules play a key role on the edge reactivity. The decomposition free energy of H_2O molecules into adsorbed H^+ and OH^- ions is computed for the different edges. For this, we calculated the dissociative adsorption energy for a single

water molecule on the edge surfaces from the explicit water layers. The formation of a Mo-O bond is observed at the Mo rich edges (ZZ-$Mo1$ and ZZ-$Mo2$) with bond distances within 2.08 to 2.30 Å. Mo sites show strong binding affinity with OH^- ions. The formation of the decomposed products on Mo rich edges are seen to be highly exothermic in nature (-1.2 and -0.9 eV respectively). On the contrary, the two S-terminated edges with 100% S-coverage (ZZ-$S1$ and ZZ-$S2$) show no uncoordinated Mo sites and are found to have endothermic energies for the decomposition of H_2O molecules. Structure with 50% S coverage (ZZ-$S1_{1/2}$ and ZZ-$S2_{1/2}$), as well as the AC edge show intermediate results. Both the surface S and Mo sites present on these edges show favorable interaction with the explicit solvent molecules. Nonetheless, decomposition on S-atoms are found to be less preferable, while water decomposition on Mo-sites is found to be almost reversible, with a decomposition free energy close to zero.

By combining the above results on stability and reactivity of the different edges in the presence of solvent molecule, it is possible to identify the most probable catalytic sites for OER. As shown above, the lower aqueous stability of ZZ-$S1$, ZZ-$S1_{1/2}$, and Mo rich edges would not allow their effective use as catalysts. Moreover, the easy oxidation of Mo-terminated edges would hinder the further reactivity of these structures with the required catalytic intermediates. The Mo site on the AC edge would also be prone to oxidation due to the fact that it is easily accessible to solvent molecules. Thus, in the following we focus our analysis on the S site of ZZ-$S2$, the S and Mo sites of ZZ-$S2_{1/2}$, and the S site of AC-MoS.

The reaction free energies are determined in acidic condition, where the reaction initiates by the adsorption of H_2O on the catalytic sites. In the CHE approach, the process is followed by four proton coupled electron transfer (PCET) intermediate steps as shown in Eqs. 1-4.[41]

$$* + H_2O \rightarrow OH^* + H^+ + e^- \ , \Delta G_1 = \Delta G_{OH^*} \tag{1}$$

$$OH^* \rightarrow O^* + H^+ + e^- \ , \Delta G_2 = \Delta G_{O^*} - \Delta G_{OH^*} \tag{2}$$

$$O^* + H_2O \rightarrow OOH^* + H^+ + e^- \ , \Delta G_3 = \Delta G_{OOH^*} - \Delta G_{O^*} \quad (3)$$

$$OOH^* \rightarrow O_2 + * + H^+ + e^- \ , \Delta G_4 = \Delta G_{O_2} - \Delta G_{OOH^*} \quad (4)$$

The free energies associated with the four steps at zero applied potential vs. SHE are denoted as ΔG_1 to ΔG_4. The first two steps involve the formation of adsorbed OH^* and O^* intermediates from H_2O on the catalyst surfaces (ΔG_1 and ΔG_2), by releasing H^+ ions and electrons. In the third step, a OOH^* intermediate forms from the interaction of the adsorbed O^* with another water molecule (ΔG_3), followed by the evolution of O_2 in the last step (ΔG_4). These free energy values are obtained from the formation free energies of the different intermediates (ΔG_{OH^*}, ΔG_{O^*} and ΔG_{OOH^*}) expressed in terms of the following electro-catalytic reactions, eqs. S4 - S6 in SI.

The reaction free energies, ΔG_1 to ΔG_4, along with the corresponding overpotential values (η) are reported in the Table 1. Table T2 (SI) shows the formation free energies ΔG_{OH^*}, ΔG_{O^*} and ΔG_{OOH^*} at the most stable adsorption sites on the basal surface and edges. In the CHE approach, the ideal catalyst is the one for which each electro-chemical step has a reaction free energy equal to the experimental redox potential of water, i.e. $\Delta G_1 = \Delta G_2 = \Delta G_3 = \Delta G_4 = 1.23$ eV. This corresponds to energy values for ΔG_{OH^*}, ΔG_{O^*} and ΔG_{OOH^*} equal to 1.23, 2.46, and 3.69 eV respectively.[5,7,42]

Compared to the ideal catalyst, the basal plane of MoS_2 shows larger oxidation potentials for OH^* and OOH^*, whereas ΔG_{O*} is reduced. The increased stability of the O^* intermediate leads to a spontaneous second catalytic step ($\Delta G_2 = -0.43$ eV). Moreover, the enhancement in binding strength for O^* reduces the interaction of the intermediate with nearby H_2O molecules and contributes to increasing the thermodynamic barrier for OOH^* formation. Due to the poor binding affinity of OOH^*, the O^* intermediate structure becomes a thermodynamic sink for the OER and ΔG_3 corresponds to the rate determining step, with an overall reaction overpotential (η) of 2.13 V.

The symmetry and structure of the ideal basal plane of MoS_2 limit the number and variety

Table 1: OER reaction free energies (ΔG, in eV) and catalytic overpotential (η, in V vs SHE) of the MoS_2 basal surface and the most relevant site of the three most stable edges in aqueous environments. The ΔG and η values are calculated using a computational hydrogen electrode (CHE) approach in presence of solvent molecules and with no external potential.

site name	ΔG				η^{sol}
	ΔG_1	ΔG_2	$\Delta G_{3/3'}$	ΔG_4	
MoS_2(basal)	1.92	-0.43	3.36	0.08	2.13
AC-MoS(S)	0.68	0.68	3.08	0.48	1.85
ZZ-$S2_{1/2}$(S)	1.21	0.69	2.89	0.12	1.66
ZZ-$S2_{1/2}$(Mo)	1.47	0.23	2.97	0.24	1.74
ZZ-S2	1.44	0.71	3.35	-0.58	2.12

of possible pathways accessible for OER, with the main one featuring all the electrochemical steps on a single S adsorption site. Considering two independent electrochemical reductions of water to O^* in nearby S atoms would involve a thermodynamic recombination step that is hindered by the high stability of the O^* intermediate. However, when considering the material's edges, the presence of different reactive sites and/or sites with partial coordination may provide additional flexibility to the catalytic process to occur at a reduced overpotential. Focusing of single site processes, it is evident from the results summarized in Table 1 that the qualitative behavior described for the basal plane also controls the catalytic activity of the edge sites. In particular, the formation of the O^* intermediate is more favorable than in the ideal catalyst, while the rate limiting step is still represented by formation of OOH^*. The ΔG_{OH^*} values are almost similar to the ideal catalyst except for AC-MoS edge, where the adsorbed hydroxyl group is more stable than the other edge sites. While the qualitative picture is similar in all the considered sites, the details of the free energies of the fours steps lead to significant differences in the overall overpotentials, which range from the highest value of 2.12 V at the ZZ-S2 edge, to the lowest value of 1.66 V for the S site of the ZZ-$S2_{1/2}$ edge.

The above results show the possibility for a reduction of the overpotential on the edges, with respect to the basal surface. Moreover, the results suggest that the morphology of

the edge and, more importantly, the elemental composition can play an important role. In particular, S atoms linked to under-coordinated Mo atoms on the edge show higher catalytic activity. In recent experiments, the MoS_2 surface has been found to be activated for OER by nano-structuring the morphology or formation of quantum dots. While these results seem in line with simulations, the computed η values are still not fully compatible with the reported experimental activities. Electro-catalytic pathways that involve more than one reaction site, structural deformation, or the rearrangement of the catalytic site may provide viable alternatives to the simplest scheme described above. Indeed, recent literature on transition metal oxide catalysts has shown that structural deformations and presence of lattice O vacancies can significantly enhance the catalytic efficiency for OER.[43]

As a matter of fact, the presence of unsatisfied valences at the MoS_2 edges might allow dramatic rearrangement of the surface atoms, thus strongly affecting the thermodynamics of the catalytic steps. While the 100% S-coverage on the most stable edge (ZZ-S2) has no accessible possibilities for surface reconstruction, several rearrangements of surface S-atoms can be characterized for the edges with reduced S concentration. In fact, each Mo atom at the edge can be associated with up to 6 S atoms, either in an individual fashion or by sharing them with the neighboring Mo atoms. A systematic screening of edge reconstructions for intermediate S-coverages and in the absence of adsorbed species shows that the most stable configuration is usually well separated in energy from alternative structures. For example, the most stable arrangement with 50% coverage (ZZ-$S2_{1/2}$ edge) corresponds to a regular structure featuring individual S atoms bridging the edge Mo-atoms as shown in Figure 1(f). Other configurations of the surface S atoms, e.g. as reported in Figure S3 (SI), result in a significant increase in the edge formation energies in vacuum and thus would not be relevant alternatives for the initial step of the catalytic process.

However, the strong binding affinity of the Mo atoms on the edge for oxygen species results in a change in stability of the reconstructed configurations in the presence of adsorbed OH^*, O^* and OOH^* intermediates. In particular, with the 50% S-coverage, one of the reconstructed

configurations denoted as 3x1(c) in Figure S3 (SI), becomes more favorable in the presence of adsorbed OH^*, O^* and OOH^* intermediates. In this reconstruction, the intermediates replace a singly bridged S atom in between two Mo-atoms, with the displaced S atom moving onto an adjacent edge position. While such a restructuring of the edge may occur at any step during the catalytic process, the significant thermodynamic barrier for the formation of the OOH^* intermediate would suggest that the process is more probable to happen during the first two catalytic steps, i.e. following the formation of the OH^* or O^*. Moreover, while the kinetic barrier for the proton transfer from the OH surface to a H_2O molecule in the aqueous layer are usually assumed to be negligible in electrochemical processes,[44] the edge reconstruction is associated with a finite kinetic energy barrier. Therefore, restructuring of the edge would be more favorable following the formation of O^* intermediate.

In Figure 3, two possible catalytic pathways, corresponding to the electrochemical step occurring on a partially or fully restructured O^* intermediate, are reported for the ZZ-$S2_{1/2}$ edge. The dashed arrows denote the steps involving thermal restructuring ($O^* \rightarrow OOH^*$), whereas the solid arrows denote the purely electrochemical steps. Figure 3(b) shows the mechanistic details of these restructuring mechanisms for the two pathways. It is important to point out that a rigid distinction between the thermal and electrochemical parts of these catalytic steps represent an approximation to a more concerted process, involving both atomic reorganization of the O^* intermediate (dotted arrows in Figure 3(b)) and charge transfers during OOH^* formation (solid arrows in Figure 3(b)). However, the distinction can significantly affect the way the overpotential is computed, as in a CHE approach only the reaction steps that involve the exchange of a proton and electron pair are affected by an applied potential. In the following, a maximum and minimum overpotential values will be reported to account for the possibility that the restructuring and the subsequent electro-catalytic step occurs in a concerted manner.

In both paths, the restructuring of the edge atoms would proceed via an intermediate state O^*_{S-Mo}, where O^* remains bonded to both S and Mo atoms as shown in Figure 3(b).

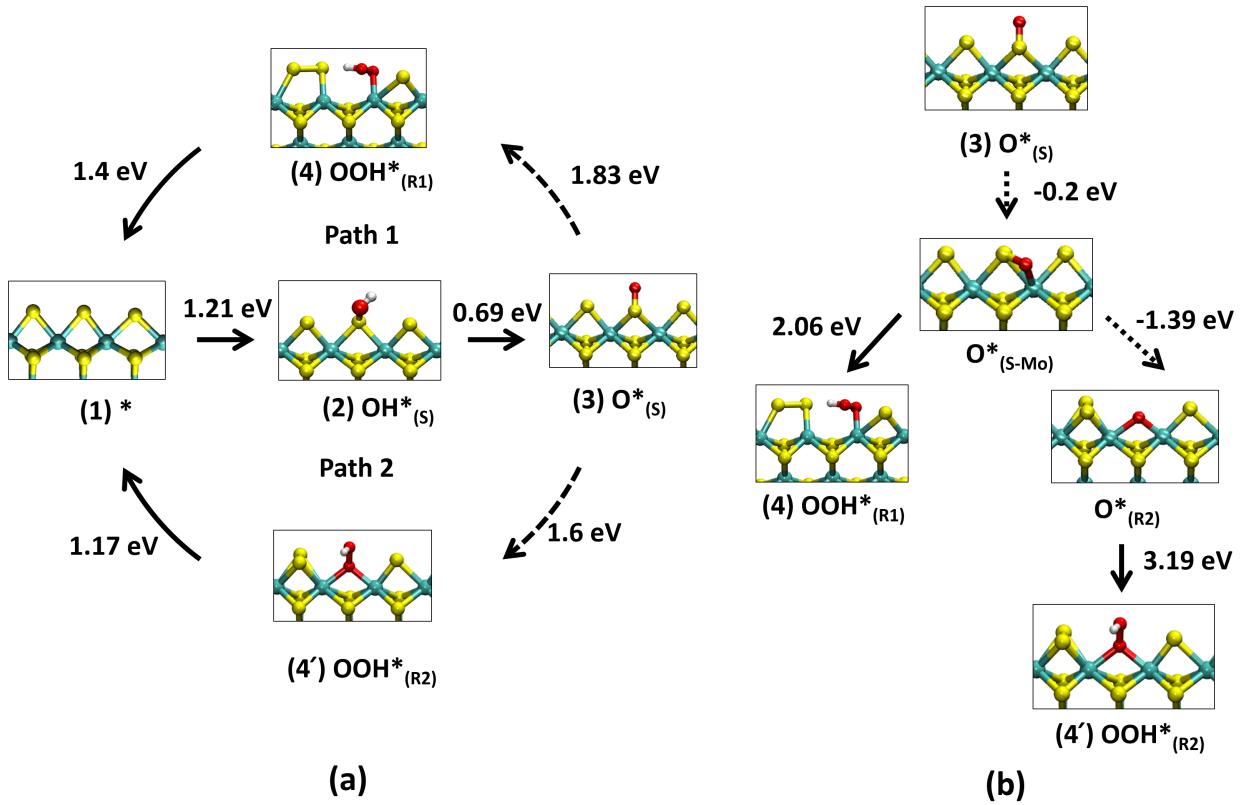

Figure 3: Details of the OER pathways for the ZZ-S$2_{1/2}$ edge and involving the displacement of the adsorbed O* intermediate. The reaction energy values for each step is shown in eV. (a) The two alternative reconstruction pathways, denoted as path 1 and path 2, differ in the OOH* formation step (ΔG_3). The steps involving both thermal rearrangement of edge atoms and electrochemical mechanisms are represented by dashed arrows, whereas the solid arrows represent the purely electrochemical steps. The restructured sites are denoted with the subscript $_{R1}$ and $_{R2}$, whereas the subscript $_S$ corresponds to the S site of un-reconstructed ZZ-S$2_{1/2}$ edge. (b) Intermediate structures involved in the rate determining step of the pathways shown in (a). The dotted arrows represent the thermal rearrangement step, whereas the solid arrows denote the electrochemical reactions and also involve the addition or removal of neutral or charged species (water molecules, hydrogen atoms, electrons, etc.) that are not reported for sake of clarity. All energies are obtained from ensemble averages of *ab* initio molecular dynamics simulations in the presence of an explicit layer of solvent molecules embedded in a continuum environment.

The ΔG for $O^*_S \rightarrow O^*_{S\text{–}Mo}$ is exothermic by 0.20 eV with a kinetic energy barrier of 0.30 eV. In the first path, the $O^*_{S\text{–}Mo}$ intermediate state would react with a water molecule, resulting in the OOH^*_{R1} intermediate. In the second path, the $O^*_{S\text{–}Mo}$ intermediate state would undergo another thermal rearrangement and form the more stable O^*_{R2} structure, before reacting with a H_2O molecule to form the OOH^*_{R2} intermediate. The kinetic energy barrier associated with the rearrangement of S-atoms in this step is found to be 0.63 eV, slightly higher than the first transition barrier. Assuming that the edge reorganization and the electrochemical step happen in a fully concerted fashion, the minimum overall reaction overpotentials associated with path 1 and 2 would be 0.60 and 0.38 V, respectively. In a non-concerted mechanism, instead, in which the exothermicity of the restructuring is uncoupled from the electrochemical reaction, these values would increase to 0.83 and 1.96 V.

While path 1 shows a significant reduction in the overall η value for the ZZ-$S2_{1/2}$ edge, in the worst case scenario, the formation of the stable bridge O^*_{R2} intermediate cannot directly improve the catalytic activity of the system. Nonetheless, such a restructuring of the edge atoms may indirectly enhance the edge's activity by providing alternative reactive sites for OER. In Figure 4, two additional reactive S-sites denoted as 1 and 2 are shown for the partially oxidized ZZ-$S2_{1/2}$ edge. Reaction free energy values at these catalytic sites can still be modeled using a 3x1 supercell, either starting from a partially oxidized ZZ-S2 edge with 33% S-coverage (shown in the blue boxes in Figure 4) or a 67% S-covered ZZ-S2 edge (as in the yellow boxes in Figure 4). Similarly to the other structures characterized so far, on both these sites the rate determining step corresponds to the formation of the OOH^* intermediates. When compared to the O^*_{R2} intermediate in site 0, for both these alternative structures the reactive O^* site is bonded to Mo atoms that have a higher coordination with electron-withdrawing atoms. This results in a weakening of the Mo-O-Mo bonds and increases the reactivity of intermediate structure. Thus, the corresponding ΔG values for the electrochemical OOH^* formation step are significantly reduced for both catalytic sites. As a result, the maximum (minimum) η values are found to be 1.02 (0.77) and 0.99 (0.72)

V vs SHE for site 1 and site 2, respectively.

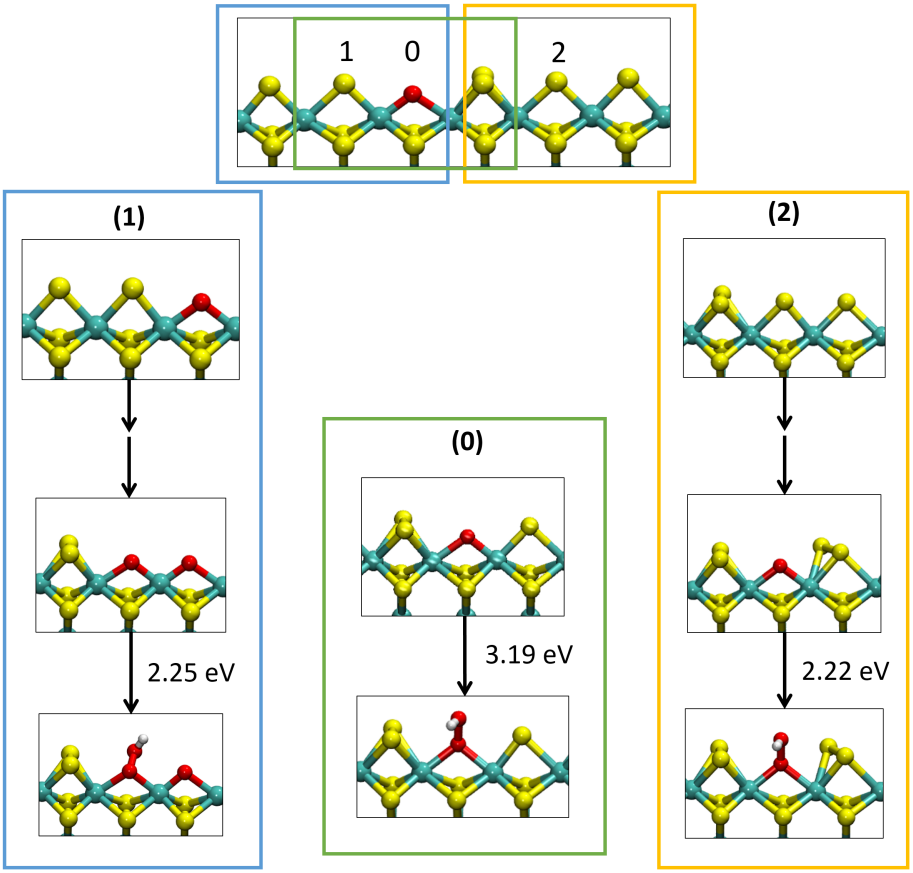

Figure 4: Catalytic active sites and OOH^* formation free energies for the restructured ZZ-$S2_{1/2}$ edge in the presence of an adsorbed O^* intermediate. In addition to the oxygen atom (labeled as site 0), nearby sulphur sites (labelled as site 1 and 2) can provide accessible catalytic pathways for the OER. The green, blue and yellow rectangular boxes represent the 3x1 simulation cells, with 50%, 33% and 66% S-coverage respectively, used to model the three reactive sites.

The above results suggest that edges with intermediate S-coverages different from 50% may also show good catalytic activity. However, it is important to note that the results obtained for the 3x1 supercells should not be considered as representative of the most stable structures of the edges, due to the constrained periodicity. In fact, the substantial stability of the symmetric bridge configuration of S atoms in the 50% system would still dominate the ZZ-S2 edges at most intermediate S coverages.

In order to further assess the catalytic activity of this edge as a function of S concentra-

tions, the $O^* \rightarrow OOH^*$ reaction on the fully oxidized ZZ-Mo2 edge has been characterized . Although in this system the Mo-O bond is weaker than in the presence of a partial S coverage, the overall edge has a more rigid structure, which hinders the deformation required to produce the OOH^* intermediate (Figure S6, SI). Thus, Mo atoms with no nearby S edge atoms are found to not be good catalytic sites, similarly to Mo atoms fully coordinated by S edge atoms (as reported in Table 1). This suggests that a non monotonic trend in the catalytic activity of the edge vs. S concentration should be observed, with maximal activity for half coverage.

Conclusions

In conclusion, the aqueous stability and catalytic activity of MoS_2 and its edges were characterized using first-principles based simulations in the presence of the solvation environment. Solvent effects appear to be significant, due to the strong affinity of the Mo atoms for oxygen. The strength of the Mo-O bond hinders the formation of the O-O bond needed to generate molecular oxygen, with the formation of the OOH^* intermediate as the rate determining step. Nonetheless, for intermediate values of the sulphur chemical potential, simulations predict the half saturated ZZ-$S2_{1/2}$ edge to be the most stable. The under coordination of the atoms at this edge of the material and the fact that different configurations are accessible to the edge S atoms introduce a flexibility that appear to be necessary to enhance the catalytic activity of the material. Following the first catalytic steps, the partially S-covered edges are seen to undergo a structural reorganization, where oxygen species bind to the edge Mo atoms. This process leads to the decrease of the OOH^* formation free energy, both for the reconstructed site and for the nearby edge sites. Overall, catalytic overpotentials comparable with experimental results are obtained for the most active structures considered. A non-monotonic behavior of the catalytic activity is predicted as a function of the sulphur coverage of the edge. These results ideally lend itself to experimental verification and can

be used to guide the design of catalytically active MoS_2-based catalytic devices.

Acknowledgement

This material is based upon work supported by the National Science Foundation (NSF) under Grant No. 1945139, under the NSF 17-537 Faculty Early Career Development Program. We acknowledge computational support and resources from the computing facilities at University of North Texas (UNT) and the Center for Advanced Scientific Computing and Modeling (CASCaM). This research used computational resources of the Compute and Data Environment for Science (CADES) cluster at the Oak Ridge National Laboratory and of the National Energy Research Scientific Computing Center (NERSC), which were supported by the Office of Science of the U.S. Department of Energy under Contract Nos. DE-AC05-00OR22725 and AC02-05CH11231, respectively.

References

(1) Deng, D.; Novoselov, K.; Fu, Q.; Zheng, N.; Tian, Z.; Bao, X. Catalysis with two-dimensional materials and their heterostructures. *Nat. Nanotechnol.* **2016**, *11*, 218–230.

(2) Chia, X.; Eng, A. Y. S.; Ambrosi, A.; Tan, S. M.; Pumera, M. Electrochemistry of nanostructured layered transition-metal dichalcogenides. *Chem. rev.* **2015**, *115*, 11941–11966.

(3) Chia, X.; Pumera, M. Layered transition metal dichalcogenide electrochemistry: journey across the periodic table. *Chem. Soc. Rev.* **2018**, *47*, 5602–5613.

(4) Li, P.; Zhu, J.; Handoko, A. D.; Zhang, R.; Wang, H.; Legut, D.; Wen, X.; Fu, Z.; Seh, Z. W.; Zhang, Q. High-throughput theoretical optimization of the hydrogen evolution reaction on MXenes by transition metal modification. *J. Mater. Chem. A* **2018**, *6*, 4271–4278.

(5) Man, I. C.; Su, H.-Y.; Calle-Vallejo, F.; Hansen, H. A.; Martinez, J. I.; Inoglu, N. G.; Kitchin, J.; Jaramillo, T. F.; Nørskov, J. K.; Rossmeisl, J. Universality in oxygen evolution electrocatalysis on oxide surfaces. *Chem Cat Chem* **2011**, *3*, 1159–1165.

(6) Han, B. Activating oxygen chemistry on metal and metal oxides: design principles of electrochemical catalysts. Ph.D. thesis, Massachusetts Institute of Technology, 2016.

(7) Nørskov, J. K.; Rossmeisl, J.; Logadottir, A.; Lindqvist, L.; Kitchin, J. R.; Bligaard, T.; Jonsson, H. Origin of the overpotential for oxygen reduction at a fuel-cell cathode. *J. Phys. Chem. B* **2004**, *108*, 17886–17892.

(8) Mak, K. F.; Lee, C.; Hone, J.; Shan, J.; Heinz, T. F. Atomically thin MoS 2: a new direct-gap semiconductor. *Phys. Rev. Lett.* **2010**, *105*, 136805.

(9) Splendiani, A.; Sun, L.; Zhang, Y.; Li, T.; Kim, J.; Chim, C.-Y.; Galli, G.; Wang, F. Emerging photoluminescence in monolayer MoS2. *Nano Lett.* **2010**, *10*, 1271–1275.

(10) Kang, J.; Tongay, S.; Zhou, J.; Li, J.; Wu, J. Band offsets and heterostructures of two-dimensional semiconductors. *Appl. Phys. Lett.* **2013**, *102*.

(11) Voiry, D.; Yamaguchi, H.; Li, J.; Silva, R.; Alves, D. C.; Fujita, T.; Chen, M.; Asefa, T.; Shenoy, V. B.; Eda, G., et al. Enhanced catalytic activity in strained chemically exfoliated WS 2 nanosheets for hydrogen evolution. *Nat. Mater* **2013**, *12*, 850–855.

(12) Jaramillo, T. F.; Jørgensen, K. P.; Bonde, J.; Nielsen, J. H.; Horch, S.; Chorkendorff, I. Identification of active edge sites for electrochemical H2 evolution from MoS2 nanocatalysts. *Science* **2007**, *317*, 100–102.

(13) Hinnemann, B.; Moses, P. G.; Bonde, J.; Jørgensen, K. P.; Nielsen, J. H.; Horch, S.; Chorkendorff, I.; Nørskov, J. K. Biomimetic hydrogen evolution: MoS2 nanoparticles as catalyst for hydrogen evolution. *J. Am. Chem. Soc.* **2005**, *127*, 5308–5309.

(14) Mohanty, B.; Ghorbani-Asl, M.; Kretschmer, S.; Ghosh, A.; Guha, P.; Panda, S. K.; Jena, B.; Krasheninnikov, A. V.; Jena, B. K. MoS2 Quantum Dots as Efficient Catalyst Materials for the Oxygen Evolution Reaction. *ACS Catal.* **2018**, *8*, 1683–1689.

(15) Sadighi, Z.; Liu, J.; Zhao, L.; Ciucci, F.; Kim, J.-K. Metallic MoS 2 nanosheets: multifunctional electrocatalyst for the ORR, OER and Li–O 2 batteries. *Nanoscale* **2018**, *10*, 22549–22559.

(16) Niyitanga, T.; Jeong, H. K. Hydrogen and oxygen evolution reactions of molybdenum disulfide synthesized by hydrothermal and plasma method. *J. Electroanal. Chem.* **2019**, *849*, 113383.

(17) Karmodak, N.; Andreussi, O. Catalytic Activity and Stability of Two-Dimensional Materials for the Hydrogen Evolution Reaction. *ACS Energy Lett.* **2020**, *5*, 885–891.

(18) Fortunelli, A.; Goddard, W. A.; Sha, Y.; Yu, T. H.; Sementa, L.; Barcaro, G.; Andreussi, O. Dramatic increase in the oxygen reduction reaction for platinum cathodes from tuning the solvent dielectric constant. *Angew. Chem. Int. Ed.* **2014**, *53*, 6669–6672.

(19) Gono, P.; Ambrosio, F.; Pasquarello, A. Effect of the Solvent on the Oxygen Evolution Reaction at the TiO2–Water Interface. *J. Phys. Chem. C* **2019**, *123*, 18467–18474.

(20) Kong, D.; Wang, H.; Cha, J. J.; Pasta, M.; Koski, K. J.; Yao, J.; Cui, Y. Synthesis of MoS2 and MoSe2 films with vertically aligned layers. *Nano Lett.* **2013**, *13*, 1341–1347.

(21) Vydrov, O. A.; Van Voorhis, T. Nonlocal van der Waals density functional made simple. *Phys. Rev. Lett.* **2009**, *103*, 063004.

(22) Vydrov, O. A.; Van Voorhis, T. Nonlocal van der Waals density functional: The simpler the better. *J. Chem. Phys.* **2010**, *133*, 244103.

(23) Sabatini, R.; Gorni, T.; De Gironcoli, S. Nonlocal van der Waals density functional made simple and efficient. *Phys. Rev. B* **2013**, *87*, 041108.

(24) Giannozzi, P., et al. Advanced capabilities for materials modelling with Quantum ESPRESSO. *J. Phys.: Condens. Matter* **2017**, *29*, 465901.

(25) Prandini, G.; Marrazzo, A.; Castelli, I. E.; Mounet, N.; Marzari, N. Precision and efficiency in solid-state pseudopotential calculations. *npj Comput. Mater.* **2018**, *4*, 72.

(26) Lejaeghere, K. et al. Reproducibility in density functional theory calculations of solids. *Science* **2016**, *351*.

(27) Andreussi, O.; Marzari, N. Electrostatics of solvated systems in periodic boundary conditions. *Phys. Rev. B* **2014**, *90*, 245101.

(28) Andreussi, O.; Dabo, I.; Marzari, N. Revised self-consistent continuum solvation in electronic-structure calculations. *J. Chem. Phys.* **2012**, *136*, 064102.

(29) Hörmann, N. G.; Guo, Z.; Ambrosio, F.; Andreussi, O.; Pasquarello, A.; Marzari, N. Absolute band alignment at semiconductor-water interfaces using explicit and implicit descriptions for liquid water. *npj Comput Mater* **2019**, *5*, 1–6.

(30) Kozbial, A.; Gong, X.; Liu, H.; Li, L. Understanding the Intrinsic Water Wettability of Molybdenum Disulfide (MoS2). *Langmuir* **2015**, *31*, 8429–8435.

(31) Chow, P. K.; Singh, E.; Viana, B. C.; Gao, J.; Luo, J.; Li, J.; Lin, Z.; Elías, A. L.; Shi, Y.; Wang, Z.; Terrones, M.; Koratkar, N. Wetting of mono and few-layered WS2 and MoS2 films supported on Si/SiO2 substrates. *ACS Nano* **2015**, *9*, 3023–3031.

(32) Gaur, A. P.; Sahoo, S.; Ahmadi, M.; Dash, S. P.; Guinel, M. J.-F.; Katiyar, R. S. Surface energy engineering for tunable wettability through controlled synthesis of MoS2. *Nano Lett.* **2014**, *14*, 4314–4321.

(33) Mills, G.; Jónsson, H. Quantum and thermal effects in H 2 dissociative adsorption: Evaluation of free energy barriers in multidimensional quantum systems. *Phys. Rev. Lett.* **1994**, *72*, 1124.

(34) Henkelman, G.; Jónsson, H. Improved tangent estimate in the nudged elastic band method for finding minimum energy paths and saddle points. *J. Chem. Phys.* **2000**, *113*, 9978–9985.

(35) Rossmeisl, J.; Skúlason, E.; Björketun, M. E.; Tripkovic, V.; Nørskov, J. K. Modeling the electrified solid–liquid interface. *Chem. Phys. Lett.* **2008**, *466*, 68–71.

(36) Skúlason, E.; Karlberg, G. S.; Rossmeisl, J.; Bligaard, T.; Greeley, J.; Jónsson, H.; Nørskov, J. K. Density functional theory calculations for the hydrogen evolution reaction in an electrochemical double layer on the Pt (111) electrode. *Phys. Chem. Chem. Phys.* **2007**, *9*, 3241–3250.

(37) Hörmann, N. G.; Andreussi, O.; Marzari, N. Grand canonical simulations of electrochemical interfaces in implicit solvation models. *J. Chem. Phys.* **2019**, *150*, 041730.

(38) Lauritsen, J. V.; Kibsgaard, J.; Helveg, S.; Topsøe, H.; Clausen, B. S.; Lægsgaard, E.; Besenbacher, F. Size-dependent structure of MoS 2 nanocrystals. *Nat. Nanotechnol.* **2007**, *2*, 53–58.

(39) Grønborg, S. S.; Salazar, N.; Bruix, A.; Rodríguez-Fernández, J.; Thomsen, S. D.; Hammer, B.; Lauritsen, J. V. Visualizing hydrogen-induced reshaping and edge activation in MoS 2 and Co-promoted MoS 2 catalyst clusters. *Nat. Commun.* **2018**, *9*, 1–11.

(40) Joo, P. H.; Cheng, J.; Yang, K. Size effects and odd-even effects in MoS2 nanosheets: First-principles studies. *Phys. Chem. Chem. Phys.* **2017**, *19*, 29927–29933.

(41) Suen, N. T.; Hung, S. F.; Quan, Q.; Zhang, N.; Xu, Y. J.; Chen, H. M. Electrocatalysis

for the oxygen evolution reaction: Recent development and future perspectives. *Chem. Soc. Rev.* **2017**, *46*, 337–365.

(42) Exner, K. S. Universality in Oxygen Evolution Electrocatalysis: High-Throughput Screening and a Priori Determination of the Rate-Determining Reaction Step. *Chem Cat Chem* **2020**,

(43) Grimaud, A.; Diaz-Morales, O.; Han, B.; Hong, W. T.; Lee, Y.-L.; Giordano, L.; Stoerzinger, K. A.; Koper, M. T.; Shao-Horn, Y. Activating lattice oxygen redox reactions in metal oxides to catalyse oxygen evolution. *Nature Chem.* **2017**, *9*, 457–465.

(44) Dickens, C. F.; Kirk, C.; Nørskov, J. K. Insights into the electrochemical oxygen evolution reaction with ab initio calculations and microkinetic modeling: beyond the limiting potential volcano. *J. Phys. Chem. C* **2019**, *123*, 18960–18977.